Magnetic properties of a spin-orbit entangled $J_{\text{eff}} = \frac{1}{2}$ honeycomb lattice

J. Khatua,[1] Q. P. Ding,[2] M. S. Ramachandra Rao,[3,4] K. Y. Choi,[5] A. Zorko,[6,7] Y. Furukawa,[2] and P. Khuntia[1,4,*]

[1]*Department of Physics, Indian Institute of Technology Madras, Chennai 600036, India*

[2]*Ames National Laboratory, U.S. DOE, and Department of Physics and Astronomy, Iowa State University, Ames, Iowa 50011, USA*

[3]*Department of Physics, Nano Functional Materials Technology Centre and Materials Science Research Centre, Indian Institute of Technology Madras, Chennai-600036, India*

[4]*Quantum Centre of Excellence for Diamond and Emergent Materials, Indian Institute of Technology Madras, Chennai 600036, India*

[5]*Department of Physics, Sungkyunkwan University, Suwon 16419, Republic of Korea*

[6]*Jožef Stefan Institute, Jamova c. 39, SI-1000 Ljubljana, Slovenia*

[7]*Faculty of Mathematics and Physics, University of Ljubljana, Jadranska u. 19, SI-1000 Ljubljana, Slovenia*

(Received 21 April 2023; revised 28 July 2023; accepted 18 August 2023; published 30 August 2023)

The interplay between spin-orbit coupling, anisotropic magnetic interaction, frustration-induced quantum fluctuations, and spin correlations can lead to novel quantum states with exotic excitations in rare-earth-based quantum magnets. Herein, we present the crystal structure, magnetization, electron spin resonance (ESR), specific heat, and nuclear magnetic resonance (NMR) experiments on the polycrystalline samples of $Ba_9Yb_2Si_6O_{24}$, in which Yb^{3+} ions form a perfect honeycomb lattice without detectable antisite disorder. The magnetization data reveal antiferromagnetically coupled spin-orbit entangled $J_{\text{eff}} = \frac{1}{2}$ degrees of freedom of Yb^{3+} ions in the Kramers doublet state. The ESR measurements reveal that the first excited Kramers doublet is 32.3(7) meV above the ground state. The specific heat results suggest the absence of any long-range magnetic order in the measured temperature range. Furthermore, the ^{29}Si NMR results do not indicate any signature of magnetic ordering down to 1.6 K, and the spin-lattice relaxation rate reveals the presence of a field-induced gap that is attributed to the Zeeman splitting of the Kramers doublet state in this quantum material. Our experiments detect neither spin freezing nor long-range magnetic ordering down to 1.6 K. The current results suggest the presence of short-range spin correlations in this spin-orbit entangled $J_{\text{eff}} = \frac{1}{2}$ rare-earth magnet on a honeycomb lattice.

DOI: 10.1103/PhysRevB.108.054442

I. INTRODUCTION

Quantum fluctuations induced by frustration, spin correlations, and spin-orbit entanglement can stabilize exotic states in quantum materials [1–3]. Understanding emergent quantum phenomena and associated elementary excitations is one of the attractive pursuits in quantum condensed matter [1–4]. The two-dimensional geometrically frustrated triangular and kagome lattices have been studied extensively to realize exotic many-body quantum phenomena such as quantum spin liquid (QSL) in condensed matter [3,5–7]. A QSL is a highly entangled state of matter wherein spins do not exhibit long-range magnetic order even at $T \to 0$ owing to strong quantum fluctuations and intertwining of competing degrees of freedom [3]. This QSL state is often characterized by exotic quasiparticle excitations such as spinons or Majorana fermions with fractional spin quantum number [8,9], which are different from the conventional magnon excitations with integer spin quantum numbers, as usually observed in magnetically ordered systems [10].

The quest for such unconventional states of matter was triggered by two theoretical scenarios. The first is the resonating valance bond state proposed by Anderson in 1973 [8]. The second one is the Kitaev QSL on the honeycomb lattice wherein $S = \frac{1}{2}$ spin is predicted to fractionalize into emergent Majorana fermions and localized Z_2 fluxes [9,11,12].

The Kitaev model on the honeycomb lattice with $J_{\text{eff}} = \frac{1}{2}$ degrees of freedom demonstrated that the bond-dependent Ising interactions provide an alternative route to realize a frustration-driven Kitaev spin-liquid state with Majorana fermions [9,13]. This has sparked significant research interest in strong spin-orbit coupled 4*d* and 5*d* honeycomb magnets, including iridates A_2IrO_3 ($A = Li^+, Na^+$) [14,15] and ruthenate α-$RuCl_3$ [2,16–18]. Beyond $4d/5d$ ion-based honeycomb magnets, the search for Kitaev materials has been extended to 3*d* transition metal Co^{2+} ion-based honeycomb compounds such as $Na_2Co_2TeO_6$ and $Na_3Co_2SbO_6$, in which oxygen ligands of 3*d* ions form nearly regular octahedra with small trigonal distortions [19,20]. Recent reports demonstrate that the combination of spin-orbit coupling and strong Hund's couplings can host pseudospin-$\frac{1}{2}$ degrees of freedom with Kitaev interactions in the aforementioned cobaltates [19,21–24]. However, most of the 3*d*-, 4*d*-, and 5*d*-based honeycomb magnets show magnetic ordering at low temperatures due to the presence of inevitable defects, site disorder, and additional exchange interactions in real materials that destabilize the Kitaev QSL ground state [25].

The essential ingredients to realize Kitaev spin liquid are spin-orbit entangled $J_{\text{eff}} = \frac{1}{2}$ moments, electron

*pkhuntia@iitm.ac.in

correlations with bond-directional Ising exchange interactions, and low dimensionality [26]. It is interesting in this respect that many recent studies have found signatures of collective quantum phenomena in low-dimensional rare-earth magnets with anisotropic interaction between pseudospin-$\frac{1}{2}$ moments [27–33].

Theoretically, it has been proposed that Yb-based honeycomb magnets may offer a more faithful realization of Kitaev physics due to strong localization and spin-orbit coupling of $4f$ electrons compared to their $4d$ or $5d$ counterparts [34–36]. In sharp contrast to the long-range Néel order state in an isotropic nearest-neighbor exchange model on the honeycomb lattice [37–42], the strong quantum fluctuations induced by further nearest-neighbor frustrated exchange interaction can destabilize the Néel order even in bipartite honeycomb lattices [43–46]. The bipartite spin lattice of rare-earth-based honeycomb magnets offers a promising venue to host spiral spin-liquid state with fracton quadrupole excitations [47,48], multiple-q states in the presence of magnetic field [49], lattice nematic phase [50], and Berezinskii-Kosterlitz-Thouless phase [51,52]. In this context, structurally perfect novel rare-earth $4f$-based honeycomb magnets wherein the combination of spin-orbit coupling and sizable crystal electric field allows for the realization of an effective spin-$\frac{1}{2}$ system with large anisotropy and strong spin correlation. These spin-orbit-driven materials offer an alternate route for the experimental search for exotic quantum many-body phenomena including Kitaev QSL [30,33,34,36,53–66].

Herein, we present our results on a promising rare-earth-based quantum magnet $Ba_9Yb_2Si_6O_{24}$, where the magnetic Yb^{3+} ions form a perfect honeycomb lattice in the *ab* plane [67]. Magnetic susceptibility data suggest the realization of a spin-orbit entangled $J_{\text{eff}} = \frac{1}{2}$ moments of Yb^{3+} ions that is consistent with a low-energy Kramers doublet state at low temperature. As revealed by electron spin resonance (ESR), the ground state is well isolated from the first excited Kramers doublet, with an energy separation of 32.3(7) meV. The Curie-Weiss fit of low-temperature magnetic susceptibility data reveals the presence of antiferromagnetic interactions in the ground state and detects neither spin glass nor long-range magnetic ordering down to 1.9 K. Specific heat measurements further support the absence of long-range magnetic order down to 1.9 K. ^{29}Si nuclear magnetic resonance (NMR) measurements in weak magnetic fields confirm the absence of long-range magnetic order in the measured temperature range. The NMR spin-lattice relaxation rate in high magnetic fields suggests the presence of a field-induced gap due to the Zeeman splitting of the lowest Kramers doublet state. Our investigation also reveals the presence of short-range spin correlations in this rare-earth honeycomb magnet.

II. EXPERIMENTAL DETAILS

Polycrystalline samples of $Ba_9Yb_2Si_6O_{24}$ (henceforth, BYSO) were prepared by a conventional solid state reaction of appropriate stoichiometry amounts of $BaCO_3$ (99.997%; Alfa Aesar), SiO_2 (99.999%; Alfa Aesar), and Yb_2O_3 (99.998%; Alfa Aesar). Prior to use, we preheated $BaCO_3$ and Yb_2O_3 at 100 °C and 800 °C, respectively, to remove moisture and carbonates. All the reagents were thoroughly ground to obtain homogeneous mixtures. The powder mixtures were pelletized and sintered at 900 °C for 24 h in air to decompose carbon dioxide. In order to obtain the desired phase, the pelletized sample was fired at 1350 °C for 72 h with several intermittent grindings. The powder x-ray diffraction (XRD) patterns were measured by employing a smartLAB Rigaku x-ray diffractometer with Cu $K\alpha$ radiation ($\lambda = 1.54$ Å). Magnetization measurements were carried out using the vibrating sample magnetometer option of a Quantum Design physical properties measurement system (QD PPMS) in the temperature range $1.9\ \text{K} \leqslant T \leqslant 300\ \text{K}$ in magnetic fields $0\ \text{T} \leqslant \mu_0 H \leqslant 7\ \text{T}$. Specific heat measurements were performed using a QD PPMS by thermal relaxation method, in the temperature range $1.9\ \text{K} \leqslant T \leqslant 250\ \text{K}$ in magnetic fields $0\ \text{T} \leqslant \mu_0 H \leqslant 7\ \text{T}$. The ESR spectrum was measured at 9.40 GHz K on a commercial X-band Bruker E500 spectrometer working at 9.40 GHz in the temperature range $4\ \text{K} \leqslant T \leqslant 140\ \text{K}$. The microwave power was varied ranging from 0.01 mW at low temperatures to 1 mW at high temperatures in order to avoid signal saturation at low temperatures and diminishing of the signal at high temperatures. To enhance the signal-to-noise ratio, the magnetic field was modulated with a frequency of 100 kHz and an amplitude of 0.5 mT, resulting in derivative ESR spectra. Field-swept ^{29}Si ($I = 1/2$, and gyromagnetic ratio 8.4577 MHz/T) NMR measurements down to 1.6 K at several frequencies were carried out on a homemade phase-coherent spin-echo pulse spectrometer equipped with a 9 T Oxford magnet. NMR spectra measurements were carried out using a standard Hahn-echo sequence while the ^{29}Si NMR spin-lattice relaxation time was extracted from the recovery of longitudinal nuclear magnetization $M(t)$ after a time delay t following a saturation pulse sequence.

III. RESULTS

A. XRD and structural details

In order to confirm the phase purity and obtain structural atomic parameters, Rietveld refinement of the x-ray diffraction data was performed using the FULLPROF suite [68]. The XRD results reveal that the polycrystalline samples of BYSO contain a small percentage of nonmagnetic Ba_2SiO_4 and magnetic Yb_2O_3 secondary phases, which do not have much effect on the overall magnetic properties of the material studied here. In the literature, it is observed that Ba_2SiO_4 (BSO) and Yb_2O_3 impurities are unavoidable in the polycrystalline samples of barium and silicon-based magnetic materials [67,69] as well as for some Yb-based magnets, respectively [70–72]. To quantify the percentage of the dominant and secondary phases, we performed a three-phase Rietveld refinement. The initial atomic coordinates were taken from Refs. [67,73] for the dominant BYSO phase and the secondary BSO phase, respectively.

Figure 1(a) depicts the Rietveld refinement of the XRD data, suggesting that our polycrystalline samples contain ≈ 94% of the dominant BYSO phase, ≈4% of the nonmagnetic BSO, and ≈2% of the magnetic Yb_2O_3 secondary phases. The Rietveld refinement reveals that BYSO crystallizes in a trigonal crystal structure with space group $R\bar{3}$. Table I lists the atomic parameters obtained from the Rietveld

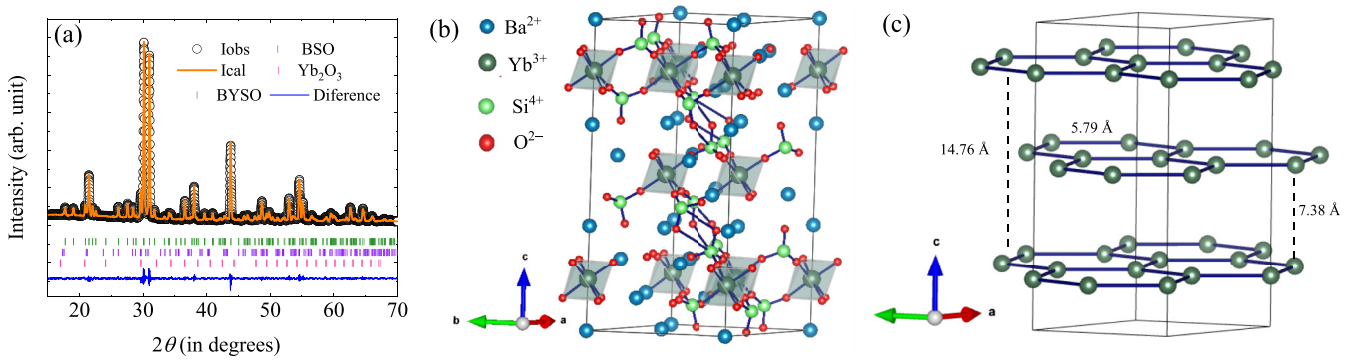

FIG. 1. (a) Rietveld refinement profile of the room-temperature x-ray diffraction data of $Ba_9Yb_2Si_6O_{24}$. The black circle represents the experimentally observed data points and the orange solid line is the calculated data. The rows of vertical bars are the Bragg reflection positions for $Ba_9Yb_2Si_6O_{24}$ (olive bars), Ba_2SiO_4 (violet bars), and Yb_2O_3 (pink bars). The blue line is the difference between observed and calculated intensities. (b) A single unit cell of the trigonal crystal structure of $Ba_9Yb_2Si_6O_{24}$. The nearest-neighbor oxygen atom of Yb^{3+} ions form a YbO_6 octahedra. The possible in-plane nearest-neighbor and interplane exchange interactions through the bridges Yb-O-Si-O-Yb and Yb-O-Si-O-Si-O-Yb are shown, respectively. (c) Structure depicting nearest-neighbor (5.79 Å) Yb^{3+} ions which form honeycomb planes. There are three such consecutive honeycomb planes in the unit cell of $Ba_9Yb_2Si_6O_{24}$.

refinement. The Yb atoms occupy only one Wyckoff atomic site 6*c* and form a six-coordinated YbO_6 octahedron with neighboring O atoms. The possible in-plane exchange interactions via Yb-O-Si-O-Yb superexchange pathways is shown in Figure 1(b). More interestingly, first nearest Yb^{3+} neighbors (5.79 Å) constitute two-dimensional honeycomb layers perpendicular to the crystallographic *c* axis and there are three such well-separated honeycomb layers in one unit cell of BYSO [Fig. 1(c)].

From the structural point of view, BYSO is a bit different from the honeycomb lattice $YbCl_3$, which crystallizes in the monoclinic crystal structure (space group $C2/m$ with lattice parameters $a = 6.732$ Å, $b = 11.620$ Å, and $c = 6.328$ Å, $\alpha = \gamma = 90.00°$, $\beta = 110.551°$) [38]. However, BYSO is structurally similar to the honeycomb lattice of $YbBr_3$, which crystallizes in the trigonal crystal structure (space group $R\bar{3}$) with the lattice parameters $a = b = 6.971$ Å, $c = 19.103$ Å, $\alpha = \beta = 90°$, and $\gamma = 120°$ [46]. Although both systems belong to the same crystal class, the ground-state properties of BYSO are expected to be different due to significant differences in the ratio of c/a and the exchange paths compared to $YbBr_3$ [46].

TABLE I. The Rietveld refinement parameters obtained from the analysis of the XRD data taken at room temperature. The Rietveld refinements were carried out with space group $R\bar{3}$ and yields unit cell parameters $a = b = 10.002$ Å, $c = 22.127$ Å, and $\alpha = 90°$, $\beta = 90°$, $\gamma = 120°$. The goodness of Rietveld refinement was confirmed by the following factors: $\chi^2 = 3.823$ and $R_{expt} = 5.25$.

Atom	Wyckoff position	*x*	*y*	*z*	Occ.
Ba_1	3*a*	0	0	0	1
Ba_2	18*f*	0.333	0.666	0.004	1
Ba_3	18*f*	0.029	0.668	0.109	1
Yb	6*c*	0	0	0.164	1
Si	18*f*	0.336	0.012	0.073	1
O_1	18*f*	0.347	0.065	0.006	1
O_2	18*f*	0.480	0.158	0.102	1
O_3	18*f*	−0.002	0.173	0.107	1
O_4	18*f*	0.137	0.468	0.094	1

B. Magnetic susceptibility

The temperature dependence of the magnetic susceptibility of BYSO in several magnetic fields is shown in Fig. 2(a). The absence of any anomaly indicates that the Yb^{3+} moment does not undergo any long-range magnetic order in the measured temperature range of investigation. The bottom inset of Fig. 2(a) depicts the zero-field-cooled (ZFC) and field-cooled (FC) susceptibility and reveals no bifurcation, which suggests the absence of spin freezing at least above 1.9 K.

Above 110 K, the inverse magnetic susceptibility data [see Fig. 2(b)] were fitted with the Curie-Weiss law, $\chi = C/(T - \theta_{CW})$, where *C* is the Curie constant and θ_{CW} is the Curie-Weiss temperature [74]. The high-temperature Curie-Weiss fit [red line in Fig. 2(b)] yields $\theta_{CW} = -111$ K and effective moment $\mu_{eff} = 4.53\mu_B$. The estimated large negative θ_{CW} is attributed to the energy scale of crystal-field excitations. The obtained effective moment $\mu_{eff} = 4.53\mu_B$ is close to that expected for free Yb^{3+} ions ($4f^{13}$; $L = 3$, $S = \frac{1}{2}$). As Yb^{3+} is a Kramers ion, generally the strong crystal electric field splits the eightfold degenerate $J = \frac{7}{2}$ multiplet into four Kramers doublets. At low temperatures, Yb^{3+} ions acquire spin-orbit entangled $J_{eff} = \frac{1}{2}$ moment. In such a scenario, the low-temperature magnetic properties are mainly governed by the exchange interactions between the $J_{eff} = \frac{1}{2}$ moment of Yb^{3+} ions in the lowest Kramers doublet state while the higher doublet states are important to understand the magnetic properties at high temperatures and high magnetic fields [75].

In order to obtain information concerning the Kramers doublet ground state and the nature of magnetic interactions, the Curie-Weiss fit to the low-temperature inverse susceptibility data is required. However, accurately estimating the actual Curie-Weiss temperature for rare-earth magnets is very crucial due to the high sensitivity of the fit parameters to the fitting range [30]. To obtain a rough idea of the Kramers doublet state and dominant magnetic interactions between Yb^{3+} moments in BYSO, the low-temperature magnetic susceptibility

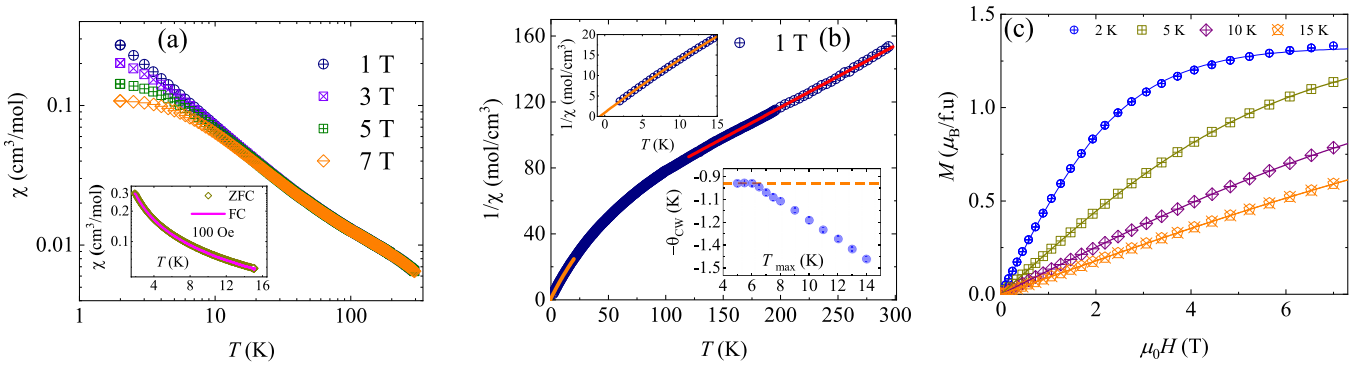

FIG. 2. (a) Temperature dependence of magnetic susceptibility in several magnetic fields. The inset (left bottom corner) shows the comparison of the zero-field-cooled (ZFC) and field-cooled (FC) magnetic susceptibility as a function of temperature in a magnetic field $\mu_0 H = 0.01$ T. (b) Temperature dependence of inverse magnetic susceptibility in a magnetic field $\mu_0 H = 1$ T with Curie-Weiss fit in the high-temperature (red line) and the low-temperature (orange line) regions. The top inset shows the Curie-Weiss fit of inverse magnetic susceptibility in the low-temperature region. The bottom inset shows the estimated Curie-Weiss temperature as a function of the upper limit of temperature range in the Curie-Weiss fit where the constant value of Curie-Weiss temperature at low temperatures is shown by a dotted orange line. (c) Isotherm magnetization as a function of magnetic field at several temperatures where the solid line represents the Brillouin function fit for paramagnetic Yb^{3+} spins with $J_{\text{eff}} = \frac{1}{2}$ moment.

data were fitted with different upper temperature limit while the lower temperature limit was fixed to 4 K as described in Ref. [30] [see the bottom inset of Fig. 2(b)]. Following this method, the temperature-independent fit parameters were found to be $\theta_{\text{CW}} = -0.94 \pm 0.01$ K and $\mu_{\text{eff}} = 2.46\mu_{\text{B}}$. The obtained value of effective moment $\mu_{\text{eff}} = 2.46\mu_{\text{B}}$ is considerably smaller than $\mu_{\text{eff}} = 4.53\mu_B$ expected for free Yb^{3+} ions. It implies the presence of a Kramer doublet state with $J_{\text{eff}} = \frac{1}{2}$ low-energy state of Yb^{3+} ions [37]. The obtained negative Curie-Weiss temperature, $\theta_{\text{CW}} = -0.94$ K, suggests the presence of a weak antiferromagnetic interaction between Yb^{3+} spins.

Figure 2(c) depicts the isothermal magnetization as a function of the magnetic field up to 7 T at several temperatures. For temperatures ($T \geqslant 2$ K) well above the interaction energy scale, one can model the observed isothermal magnetization following the Brillouin function, $M/M_s = B_{1/2}(y)$, where $B_J(y) = \{\frac{2J+1}{2J}\coth[\frac{y(2J+1)}{2J}] - \frac{1}{2J}\coth\frac{y}{2J}\}$ is the Brillouin function, M_s $(= gJ\mu_B)$ is the saturation magnetization, and $y = g\mu_B J\mu_0 H/k_B T$ is the ratio of the Zeeman energy of magnetic moment to the thermal energy, μ_B is the Bohr magneton, and g is the Landé g factor. The solid lines in Fig. 2(c) for 2, 5, 10, and 15 K are the Brillouin function fit which yields an average Landé g factor, $g = 2.45$, while J was fixed to $\frac{1}{2}$, consistent with the lowest Kramers doublet state of Yb^{3+} ions in this temperature regime.

C. Electron spin resonance

ESR measurements were performed on the powder sample of BYSO at $T \geqslant 4$ K. The ESR spectra exhibit pronounced broadening with increasing temperature, making the signal too broad for reliable analysis above 140 K [Fig. 3(a)]. Below 50 K, the spectra become structured; however, their line shape does not correspond to a single powder pattern due to anisotropic g factors. Above 70 K, the spectra can be nicely fitted with a single Lorentzian curve, revealing motional narrowing effects on the line shape [76].

The temperature dependence of the ESR linewidth [Fig. 3(b)] is due to crystal-electric-field (CEF) fluctuations, as often encountered in rare-earth magnets [30], where excited CEF levels are relatively low in energy. The broadening is due to the Orbach process, involving two-phonon scattering via excited CEF levels [77]. Indeed, the experimental linewidth ΔB is well described with the expression $\Delta B(T) = \Delta B_0 + \{f/[\exp(\Delta/k_B T) - 1]\}$, where the constant term ΔB_0 arises from the magnetic anisotropy in the CEF ground state, while the exponential term describes the Orbach relaxation with f being the scaling factor between the ESR linewidth and the spin fluctuation frequency, and Δ being the energy gap between the CEF ground state and the lowest excited state. The fit of the model to the experimental data yields $\Delta B_0 = 51(3)$ mT, $f = 13(1)$ T, and $\Delta = 32.3(7)$ meV. This gap value is very similar to the gap of 39.4 meV observed in $YbMgGaO_4$ [78] or 34.8 meV observed in $NaYbO_2$ [79]. Both materials possess YbO_6 octahedra with frustrated two-dimensional arrangements, similar to BYSO.

D. Specific heat

In order to gain further insights into ground-state properties, we performed the temperature dependence of specific heat $[C_{\text{p}}(T)]$ of BYSO down to 1.9 K in several magnetic fields up to 7 T. The temperature dependence of zero-field C_{p}/T data in the temperature range 1.9 K $\leqslant T \leqslant$ 250 K is shown in Fig. 4(a). It is noted that in zero magnetic field an anomaly appears at $T_{\text{N}} = 2.26$ K that is attributed to the transition temperature of the unreacted minor impurity phase of Yb_2O_3 in BYSO [Fig. 4(b)] [70,71,80,81]. However, the Yb^{3+} moments decorating the two-dimensional honeycomb lattice do not undergo long-range magnetic order down to 1.9 K.

In order to extract the magnetic specific heat associated with Yb^{3+} spins from the total specific heat, we model the lattice contribution due to phonons using the Debye function, i.e., $C_{\text{lat.}}(T) = 9k_B[\sum_{n=1}^{2} C_n(\frac{T}{\theta_{D_n}})^3 \int_0^{\theta_{D_n}/T} \frac{x^4 e^x}{(e^x-1)^2} dx]$, where θ_D

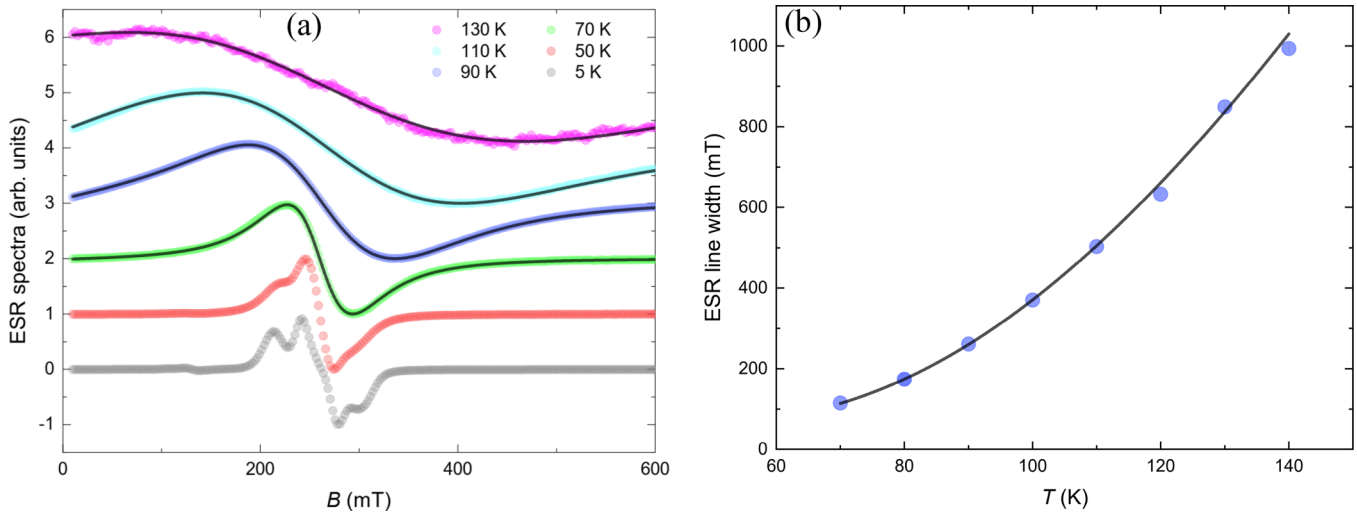

FIG. 3. (a) The ESR spectra of $Ba_9Yb_2Si_6O_{24}$ at various temperatures (circles), with corresponding best fits with isotropic Lorentzian line shape (solid lines) above 70 K. The spectra are shifted vertically for clarity. (b) The temperature dependence of the ESR linewidth (circles), with the solid line representing the fit to the Orbach model, yielding the energy gap of $\Delta = 32.3(7)$ meV (see text for details).

is the Debye temperature, while R and k_B are the molar gas constant and Boltzmann constant, respectively. The solid red line in Fig. 4(a) is the fitted lattice contributions that were obtained with $\theta_{D1} = 234$ K and $\theta_{D2} = 456$ K. In the fits, two coefficients were fixed in the ratio $C_{D1} : C_{D2} = 17 : 24$ that corresponds to the ratio of the number of heavy and light atoms in BYSO [82–84]. The associated magnetic contribution $C_{\rm mag}(T)$ was extracted after subtracting lattice contribution and is shown in Fig. 4(c) as a function of temperature.

The temperature dependence of $C_{\rm p}(T)/T$ in magnetic fields up to 7 T is shown in Fig. 4(b). In a magnetic field of 3 T, only a broad maximum is observed around 2.3 K in the specific heat while the anomaly due to Yb_2O_3 is fully suppressed. This observation suggests that the low-field specific heat data most likely show a broad maximum at substantially lower temperatures due to the weak exchange coupling between $J_{\rm eff} = \frac{1}{2}$ moments of Yb^{3+} ions [86,87]. Above 3 T, this broad maximum progressively shifts toward higher temperatures and it behaves like a Schottky anomaly, suggesting the presence of a field-polarized state with a field-induced gap in high magnetic fields [36]. A similar scenario has been suggested in the honeycomb lattice $YbCl_3$ [39] and other low-dimensional frustrated magnets [27,88]. In BYSO, the field-induced gap is attributed to the Zeeman splitting of the lowest Kramers doublet state, effectively surpassing the intrinsic exchange interactions between $J_{\rm eff} = \frac{1}{2}$ moments in the ground-state Kramers doublet. To estimate the gap value, the high-field magnetic specific heat data were fitted with a two-level Schottky expression of the specific heat,

$$C_{\rm Sch.} = fR\left(\frac{\Delta_s}{k_BT}\right)^2 \frac{\exp(\Delta_s/k_BT)}{[1+\exp(\Delta_s/k_BT)]^2}, \qquad (1)$$

where $\Delta_{\rm s}$ is the gap induced by the Zeeman splitting of the ground-state Kramers doublet of a Yb^{3+} ion, and f measures the fraction of Yb^{3+} spins which contribute to the splitting of the ground-state doublet. The fitted solid lines in Fig. 4(c) were obtained using Eq. (1). Figure 5(e) displays the corresponding estimated field-induced gap. The estimated gap value is consistent with that obtained from nuclear magnetic

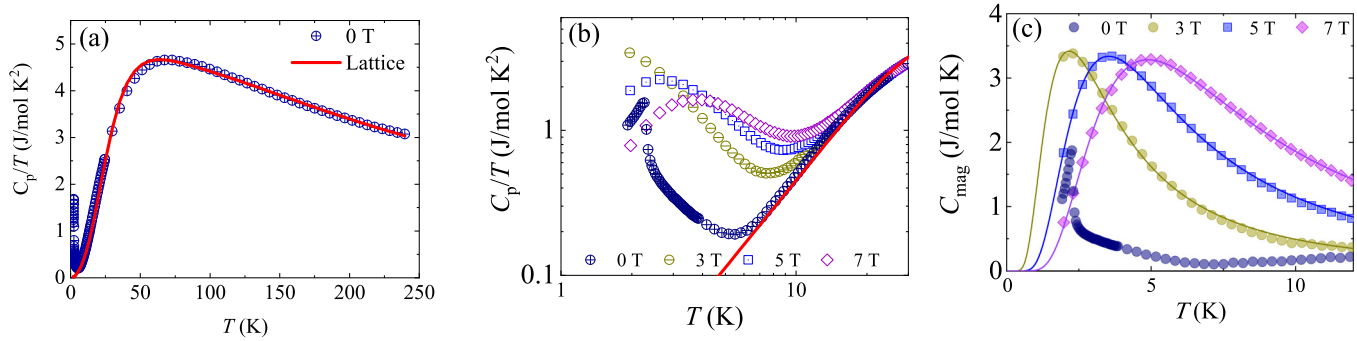

FIG. 4. Temperature dependence of zero-field specific heat divided by temperature, $C_{\rm p}/T$, where the red line is the fitting curve by the Debye model (see text) which accounts for phonon contributions. (b) Temperature dependence of $C_{\rm p}/T$ in several magnetic fields. The anomaly at $\sim T = 2.26$ K in zero field corresponds to the transition temperature of the minor impurity phase of Yb_2O_3 in BYSO. (c) Temperature dependence of magnetic specific heat in several magnetic fields where the solid line depicts the fit using Eq. (1).

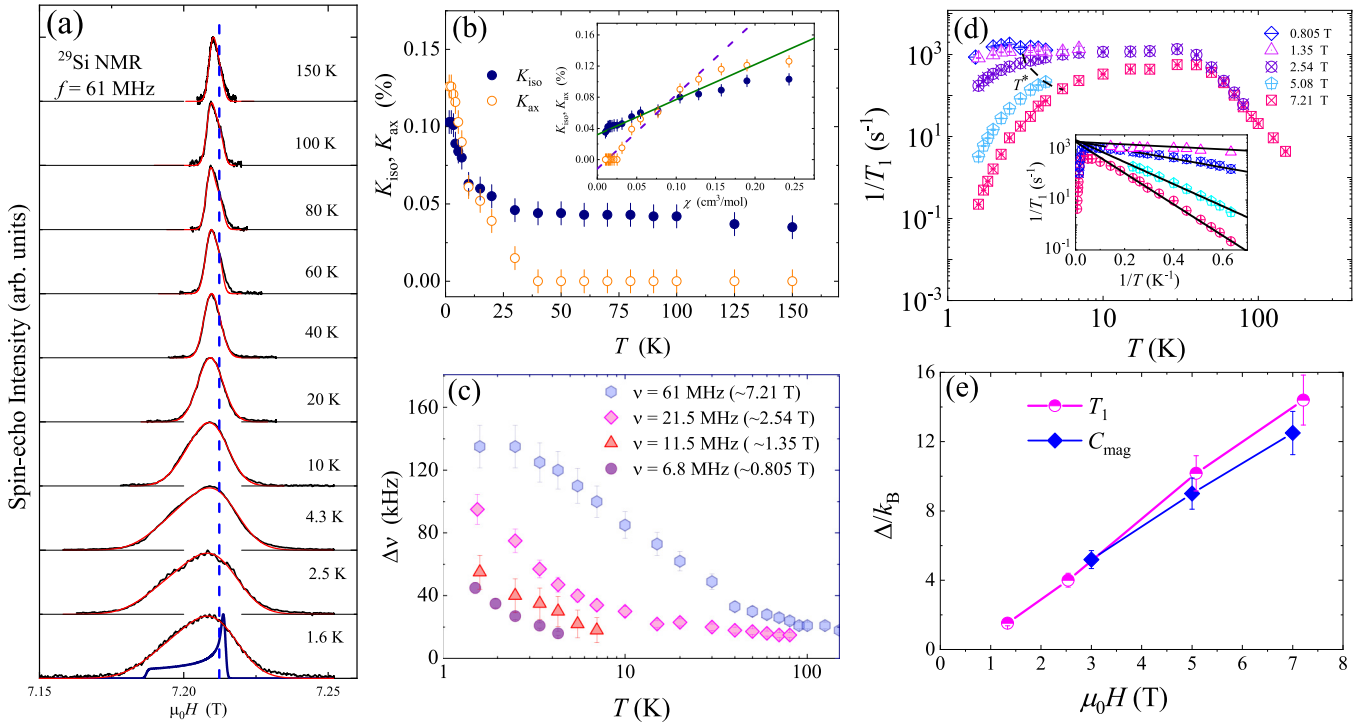

FIG. 5. The field-swept ^{29}Si-NMR spectra measured at a constant frequency $\nu = 61$ MHz at various temperatures. The blue dashed vertical line corresponds to the zero-shift reference position of 7.2123 T. The blue curve at the bottom shows the calculated asymmetric NMR spectrum due to hyperfine anisotropy (K_{iso} and K_{ax}) with nearly zero inhomogeneous magnetic broadening at $T = 1.6$ K. The red curves are calculated spectra by taking into consideration the inhomogeneous magnetic broadening introduced by convoluting the Lorentzian function with the full width at half maximum defined as a parameter $\Delta\nu$. The slightly asymmetric shape in the spectra at higher temperatures above ~60 K is probably due to the ^{29}Si NMR signal at the zero-shift position from the nonmagnetic impurity of Ba_2SiO_4 [85]. (b) Temperature dependence of K_{iso} and K_{ax}. The inset shows K_{iso} and K_{ax} versus magnetic susceptibility χ. The solid and dashed lines are linear fits, $K_{iso} = 0.45\chi + 0.032$ and $K_{ax} = 0.95\chi - 0.012$, respectively, with units of percent for NMR shifts and cm^3/mol for magnetic susceptibility. (c) The temperature dependence of $\Delta\nu$ (inhomogeneous magnetic broadening) determined by the simulation of the NMR spectra measured at different frequencies (i.e., different magnetic field). (d) The temperature dependence of the ^{29}Si NMR spin-lattice relaxation rate ($1/T_1$) measured at five different fields on a log-log scale. The inset shows the $1/T_1$ as a function of inverse temperature ($1/T$) for different magnetic fields on a semilogarithmic scale. The black lines in the inset represent the fits with a phenomenological model valid for thermally activated behavior of $1/T_1$ as discussed in the text. (e) Magnetic field dependence of the magnitude of the field-induced gap estimated from the $1/T_1$ and heat capacity measurements.

resonance spin-lattice relaxation experiments [see Fig. 5(d)]. The estimated fraction of Yb^{3+} spins was close to 1, suggesting that almost all the Yb^{3+} spins contribute to the observed effect [83,89]. The spin correlations between $4f$ moments generally develop at low temperature in view of the weak exchange interaction between magnetic moments in these materials. This calls for sub-Kelvin thermodynamic experiments to gain deeper insights into the ground state of this $4f$-based honeycomb antiferromagnet [90].

E. Nuclear magnetic resonance

In order to track the intrinsic static magnetic susceptibility and spin dynamics of BYSO, we also performed NMR measurements on ^{29}Si (nuclear spin $I = \frac{1}{2}$, gyromagnetic ratio $\gamma_N/2\pi = 8.4577$ MHz/T). Figure 5(a) shows the field-swept ^{29}Si NMR spectra at several temperatures at $\nu = 61$ MHz. The smooth evolution of the field-swept NMR spectra in the entire temperature range without developing rectangular shape or splitting of the ^{29}Si line suggests the absence of long-range magnetic ordering in the compound [91–93].

At high temperatures, the NMR spectra are relatively narrow, but as the temperature drops, they start widening and exhibit anisotropic behavior at low temperatures. The asymmetric shapes of the spectra were well reproduced by the calculated spectra where we introduced an anisotropy in NMR shift K. The red curves in Fig. 5(a) show the calculated powder-pattern spectra with isotropic and axial components of NMR shifts (K_{iso} and K_{ax}), which reproduced the observed spectra well. Here, we calculated the spectra by taking into consideration the short-range spin correlations that cause inhomogeneous magnetic broadening, which is introduced by convoluting the Lorentzian function with the full width at half maximum defined as a parameter $\Delta\nu$. The blue curve at the bottom shows the calculated asymmetric NMR spectrum due to hyperfine anisotropy (K_{iso} and K_{ax}) with nearly zero inhomogeneous magnetic broadening at $T = 1.6$ K. The NMR shift K is described by $K = K_{iso} + K_{ax}(3\cos^2\theta - 1)$, where θ is the angle between the principal axis of the hyperfine tensor at the Si site and the external magnetic field. At higher temperatures above ~60 K, the relatively narrow spectra also show slightly asymmetric shapes but with tails on the higher magnetic field side, in contrast to those observed

at low temperatures. From the detailed analysis, it turned out that the slightly asymmetric shape of the spectra at higher temperatures above ~60 K can be explained by an additional ^{29}Si NMR signal at the zero-shift position [the red curves in Fig. 5(a) for $T > 60$ K] which is probably due to the signal from the nonmagnetic impurity of Ba_2SiO_4 [85].

Figure 5(b) shows the temperature dependence of K_{iso} and K_{ax} determined by fitting the spectra. K_{iso} and K_{ax} are nearly independent of temperature within our experimental uncertainty above 40 K; however, both show a clear increase below ~40 K beyond our experimental uncertainty. It is interesting to point out that 40 K is close to the crossover temperature between the $J_{eff} = \frac{1}{2}$ and $J = \frac{7}{2}$ states as shown in the magnetic susceptibility measurements (see Fig. 2). Below 7 K, both K_{iso} and K_{ax} saturate to finite values, whose behavior is ascribed to the strong polarization of the Yb^{3+} moments in high magnetic fields. The obtained NMR shift can be expressed as $K(T) = K_0 + K_{spin}(T) = K_0 + (A_{hf}/N_A\mu_B)\chi(T)$, where the first term ($K_0$) represents the sum of temperature-independent contribution arising from the orbital susceptibility and chemical shift, and the second term is the spin part of K which accounts for the temperature-dependent intrinsic spin susceptibility of Yb^{3+} spins. Here A_{hf} is the hyperfine coupling constant, and N_A the Avogadro number. To extract the hyperfine coupling constants, the NMR shifts versus magnetic susceptibility (at 1 T) were plotted with temperature as an implicit parameter in the inset of Fig. 5(b) (also known as the Clogston-Jaccarino plot) [94]. From the linear fit in the temperature range of $T = 7$–150 K, A_{hf} and K_0 are estimated to be $A_{hf,iso} = 25 \pm 3$ Oe/μ_B and $K_{0,iso} = 0.032\%$ for the isotropic part and $A_{hf,ax} = 53 \pm 10$ Oe/μ_B and $K_{0,ax} = -0.012\%$ for the axial part, respectively.

The broadening of NMR spectra with decreasing temperature is due to the increase of the distributions in K_{ax} and K_{iso}. The temperature and magnetic field dependence of the inhomogeneous broadenings is shown in Fig. 5(c), where $\Delta\nu$ is plotted as a function of temperature. $\Delta\nu$ depends on temperature and increases with increasing magnetic field. This is consistent with the magnetization measurements since $\Delta\nu$ is related to the magnetization.

The NMR spin-lattice relaxation rate (T_1^{-1}) probes the low-energy spin excitations related to the dynamic spin susceptibility governed by fluctuations of electron spin at the nuclear sites through hyperfine interactions. Figure 5(d) depicts the temperature dependence of T_1^{-1} with three distinct regions of different spin-lattice relaxation rates. In the entire temperature range of investigation, the relaxation rates were estimated from fitting the recovery of longitudinal nuclear magnetization $M(t)$ by a single exponential function, $M_z(t) = [M_0 - M(t)]/M_0 = A\exp(-t/T_1)$, where M_0 is the equilibrium magnetization, $M_z(t)$ is the magnetization at time t after the saturation pulse, and A is a constant. It is noted that all measured relaxation curves were well fitted with a single component of T_1, implying a homogeneous distribution of spin-lattice relaxation rates in this $4f$ honeycomb lattice system. Upon cooling, the T_1^{-1} increases until the plateau around 50 K in magnetic fields $\mu_0 H = 2.5$ and 7.2 T. This behavior is often observed in rare-earth magnets due to the depopulation of the crystal electric field and is due to the Orbach mechanism that is responsible for the ESR line broadening in BYSO [86].

Below 50 K, T_1^{-1} first remains nearly temperature independent down to a field-dependent characteristic temperature, as shown by the dotted curve in Fig. 5(d). Although T_1^{-1} slightly decreases with decreasing temperature in a high magnetic field of 7.2 T, the nearly temperature-independent behavior of T_1^{-1} in the intermediate temperature range suggests that the relaxation rate is dominated by the paramagnetic spin fluctuations of Yb^{3+} spins in the crystal field ground state. One can expect the correlated magnetism of Yb^{3+} spins and a field-polarized phase at low temperatures owing to the weak exchange interaction between Yb^{3+} spins typical for rare-earth-based quantum magnets [83]. The relaxation rate T_1^{-1} decreases rapidly below the characteristic temperature T^*, suggesting that the applied magnetic field opens a gap which normally occurs when the Zeeman energy exceeds the interaction energy between Yb^{3+} ions. To estimate the value of the gap in the presence of a magnetic field, we present T_1^{-1} as a function of inverse temperature in a semilogarithmic plot for $\mu_0 H > 1.35$ T as shown in the inset of Fig. 5(d). The solid line represents the fit to the experimental data using the phenomenological model relevant for thermally activated behavior of magnetic moments, i.e., $T_1^{-1} \propto \exp(-\Delta_s/k_B T)$, where Δ_s is the gap value to the Zeeman splitting of the ground-state Kramers doublet in the presence of a magnetic field. We find a linear variation of the gap with the applied magnetic field [see Fig. 5(e)], as expected when the Zeeman energy overcomes the exchange energy. The estimated Δ_s from the NMR measurements is in good agreement with the gap values obtained from the specific heat measurements [Fig. 4(c)].

IV. DISCUSSION

In this work, we have investigated crystal structure and ground-state properties of an unexplored rare-earth-based honeycomb spin-lattice $Ba_9Yb_2Si_6O_{24}$ through the combination of thermodynamic and microscopic measurements. $Ba_9Yb_2Si_6O_{24}$, nearly free from antisite disorder, constitutes a perfect honeycomb lattice of Yb^{3+} ions perpendicular to the crystallographic c axis. Magnetic susceptibility data suggest the presence of spin-orbit entangled $J_{eff} = \frac{1}{2}$ moments of Yb^{3+} ions with a Kramers doublet ground state, which are exchange coupled by weak antiferromagnetic interactions at low temperatures. The mean-field formula $\theta_{CW} = [-zJS(S+1)]/3k_B$ offers an approximate estimation of the exchange interaction J/k_B between $J_{eff} = \frac{1}{2}$ moments of Yb^{3+} ions in the ab plane taking into account the nearest-neighbor $z = 3$ and $S = J_{eff} = \frac{1}{2}$ for BYSO [95]. The nearest-neighbor exchange interaction in the ab plane is found to be roughly 1.3 K while the dipolar interaction energy $E_{dip} \approx \mu_0 g_{avg}^2 \mu_B^2/4\pi a^3 \approx 0.3\%$ of the nearest-neighbor exchange interactions, where g_{avg} is the powder average Landé g factor and a is the nearest-neighbor Yb-Yb bond length in BYSO. This implies the presence of a significant superexchange interaction between $J_{eff} = \frac{1}{2}$ moments of Yb^{3+} ions in BYSO in addition to the dipolar interaction, analogous to the honeycomb lattice $YbBr_3$ [46]. In contrast to the corner and side-sharing regular $YbBr_6$ octahedra in the two-dimensional honeycomb lattice $YbBr_3$, YbO_6 octahedra in BYSO are isolated [46]. Thus,

in BYSO, the nearest-neighbor intraplane superexchange interaction can only occur via the Yb-O-Si-O-Yb virtual path, which may be one of the reasons for the weak antiferromagnetic interaction strength between Yb^{3+} moments in BYSO. Contrarily, in $YbBr_3$, the bromine ion directly mediates the nearest-neighbor superexchange interaction through the Yb-Br-Yb virtual electron hopping processes, which results in a little higher interaction strength ($\approx$8 K) [46]. Furthermore, in BYSO, the nature of exchange interactions between Yb^{3+} moments is expected to be Heisenberg type as the YbO_6 octahedra are connected through intermediate Si^{4+} ions which prevent one of the essential requirements, i.e., Yb-O-Yb bond angles of 90° for stabilizing Kitaev interactions [see Fig. 1(b)] [96].

Our ESR results indicate the presence of anisotropic magnetic interaction between $J_{\text{eff}} = \frac{1}{2}$ moments of Yb^{3+} ions. Normally, in the conventional antiferromagnetically ordered state, the crystallographic site of the probing nucleus in an NMR experiment becomes inequivalent and senses different magnetic fields which leads to splitting the NMR spectra when internal fields at the nucleus are parallel or antiparallel to an external magnetic field. The absence of NMR line splitting or rectangular spectra confirms the absence of long-range magnetic order in BYSO down to 1.6 K, which substantiates that the minor Yb_2O_3 impurity phase does not significantly affect the underlying magnetic properties of the material under consideration. The bulk of the material maintains a dynamic ground state at least down to 1.6 K. In high magnetic fields, the exponential decay of the spin-lattice relaxation rate at low temperature is attributed to a field-induced gap due to the Zeeman splitting of the low-energy Kramers doublet state, which typically takes place when the Zeeman energy exceeds the exchange interaction energy. Theoretically, it has been suggested that the competing magnetic interactions between nearest-neighbor and next-neighbor Yb^{3+} ions can nevertheless lead to the realization of a quantum spin-liquid state in honeycomb lattices even in the absence of Kitaev-type interactions [42,97–99]. The two-dimensional honeycomb lattice BYSO seems promising in this direction, and its low-temperature magnetic properties on single crystal could hold significant potential for future investigations.

V. SUMMARY

To summarize, we have synthesized and performed magnetization, specific heat, ESR, and NMR experiments on a $4f$ electron-based material $Ba_9Yb_2Si_6O_{24}$, which crystallizes in a trigonal crystal structure with the space group $R\bar{3}$. In this material, the Yb^{3+} ions constitute a perfect honeycomb lattice in the ab plane. Magnetization data suggest the pseudospin-$\frac{1}{2}$ degrees of freedom of Yb^{3+} ions in the Kramers doublet state, and these $J_{\text{eff}} = \frac{1}{2}$ spins interact antiferromagnetically. The lowest CEF excited Kramers doublet is far above [at 32.3(7) meV] the ground state, as estimated from ESR.

The absence of long-range magnetic ordering between pseudospin-$\frac{1}{2}$ moments of Yb^{3+} ions in specific heat data, which is corroborated by microscopic NMR results down to 1.6 K, suggests that the two-dimensional honeycomb lattice $Ba_9Yb_2Si_6O_{24}$ can host a spin-liquid ground state. The spin-lattice relaxation rate measurements in high magnetic fields show the presence of a field-induced gap due to Zeeman splitting of the Kramers doublet, which is consistent with specific heat results. Further studies on single crystals of $Ba_9Yb_2Si_6O_{24}$ are highly desired to shed more insight into the anisotropic magnetic interactions and low-energy excitations. The present family of rare-earth-based honeycomb spin-lattice $Ba_9R_2Si_6O_{24}$ (R = rare-earth ions) with distinct rare-earth elements, spin-orbit-driven anisotropy, and spin correlations provide an ideal ground to realize exotic quantum phenomena.

ACKNOWLEDGMENTS

P.K. acknowledges funding by the Science and Engineering Research Board and Department of Science and Technology, India through research grants. This research was supported by the U.S. Department of Energy, Office of Basic Energy Sciences, Division of Materials Sciences and Engineering. Ames National Laboratory is operated for the U.S. Department of Energy by Iowa State University under Contract No. DEAC02-07CH11358. A.Z. acknowledges the financial support of the Slovenian Research Agency through Program No. P1-0125 and Projects No. N1-0148 and No. J1-2461.

[1] W. Witczak-Krempa, G. Chen, Y. B. Kim, and L. Balents, Annu. Rev. Condens. Matter Phys. **5**, 57 (2014).
[2] H. Takagi, T. Takayama, G. Jackeli, G. Khaliullin, and S. E. Nagler, Nat. Rev. Phys. **1**, 264 (2019).
[3] L. Balents, Nature (London) **464**, 199 (2010).
[4] P. Khuntia, J. Magn. Magn. Mater. **489**, 165435 (2019).
[5] P. Khuntia, M. Velazquez, Q. Barthélemy, F. Bert, E. Kermarrec, A. Legros, B. Bernu, L. Messio, A. Zorko, and P. Mendels, Nat. Phys. **16**, 469 (2020).
[6] C. Broholm, R. J. Cava, S. A. Kivelson, D. G. Nocera, M. R. Norman, and T. Senthil, Science **367**, eaay0668 (2020).
[7] J. Wen, S.-L. Yu, S. Li, W. Yu, and J.-X. Li, npj Quantum Mater. **4**, 12 (2019).
[8] P. W. Anderson, Mater. Res. Bull. **8**, 153 (1973).
[9] A. Kitaev, Ann. Phys. **321**, 2 (2006).
[10] K. Matan, D. Grohol, D. G. Nocera, T. Yildirim, A. B. Harris, S. H. Lee, S. E. Nagler, and Y. S. Lee, Phys. Rev. Lett. **96**, 247201 (2006).
[11] Y. Motome and J. Nasu, J. Phys. Soc. Jpn. **89**, 012002 (2020).
[12] G. Baskaran, S. Mandal, and R. Shankar, Phys. Rev. Lett. **98**, 247201 (2007).
[13] K. Kitagawa, T. Takayama, Y. Matsumoto, A. Kato, R. Takano, Y. Kishimoto, S. Bette, R. Dinnebier, G. Jackeli, and H. Takagi, Nature (London) **554**, 341 (2018).
[14] S. K. Choi, R. Coldea, A. N. Kolmogorov, T. Lancaster, I. I. Mazin, S. J. Blundell, P. G. Radaelli, Y. Singh, P. Gegenwart, K. R. Choi, S.-W. Cheong, P. J. Baker, C. Stock, and J. Taylor, Phys. Rev. Lett. **108**, 127204 (2012).
[15] J. Chaloupka, G. Jackeli, and G. Khaliullin, Phys. Rev. Lett. **105**, 027204 (2010).

[16] K. W. Plumb, J. P. Clancy, L. J. Sandilands, V. V. Shankar, Y. F. Hu, K. S. Burch, H.-Y. Kee, and Y.-J. Kim, Phys. Rev. B **90**, 041112(R) (2014).

[17] J. A. Sears, L. E. Chern, S. Kim, P. J. Bereciartua, S. Francoual, Y. B. Kim, and Y.-J. Kim, Nat. Phys. **16**, 837 (2020).

[18] A. Banerjee, C. A. Bridges, J.-Q. Yan, A. A. Aczel, L. Li, M. B. Stone, G. E. Granroth, M. D. Lumsden, Y. Yiu, J. Knolle, S. Bhattacharjee, D. L. Kovrizhin, R. Moessner, D. A. Tennant, D. G. Mandrus, and S. E. Nagler, Nat. Mater. **15**, 733 (2016).

[19] H. Liu and G. Khaliullin, Phys. Rev. B **97**, 014407 (2018).

[20] H. Liu, J. Chaloupka, and G. Khaliullin, Phys. Rev. Lett. **125**, 047201 (2020).

[21] C. Kim, J. Jeong, G. Lin, P. Park, T. Masuda, S. Asai, S. Itoh, H.-S. Kim, H. Zhou, J. Ma, and J.-G. Park, J. Phys.: Condens. Matter **34**, 045802 (2022).

[22] M. Songvilay, J. Robert, S. Petit, J. A. Rodriguez-Rivera, W. D. Ratcliff, F. Damay, V. Balédent, M. Jiménez-Ruiz, P. Lejay, E. Pachoud, A. Hadj-Azzem, V. Simonet, and C. Stock, Phys. Rev. B **102**, 224429 (2020).

[23] Y. Motome, R. Sano, S. Jang, Y. Sugita, and Y. Kato, J. Phys.: Condens. Matter **32**, 404001 (2020).

[24] P. P. Stavropoulos, D. Pereira, and H.-Y. Kee, Phys. Rev. Lett. **123**, 037203 (2019).

[25] F. Bahrami, M. Abramchuk, O. I. Lebedev, and F. Tafti, Molecules **27**, 871 (2022).

[26] S. Trebst and C. Hickey, Phys. Rep. **950**, 1 (2022).

[27] L. S. Wu, S. E. Nikitin, Z. Wang, W. Zhu, C. D. Batista, A. M. Tsvelik, A. M. Samarakoon, D. A. Tennant, M. Brando, L. Vasylechko, M. Frontzek, A. T. Savici, G. Sala, G. Ehlers, A. D. Christianson, M. D. Lumsden, and A. Podlesnyak, Nat. Commun. **10**, 698 (2019).

[28] Y. Li, H. Liao, Z. Zhang, S. Li, F. Jin, L. Ling, L. Zhang, Y. Zou, L. Pi, Z. Yang, J. Wang, Z. Wu, and Q. Zhang, Sci. Rep. **5**, 16419 (2015).

[29] Y. Li, D. Adroja, P. K. Biswas, P. J. Baker, Q. Zhang, J. Liu, A. A. Tsirlin, P. Gegenwart, and Q. Zhang, Phys. Rev. Lett. **117**, 097201 (2016).

[30] T. Arh, B. Sana, M. Pregelj, P. Khuntia, Z. Jagličić, M. D. Le, P. K. Biswas, P. Manuel, L. Mangin-Thro, A. Ozarowski, and A. Zorko, Nat. Mater. **21**, 416 (2022).

[31] Z. Dun, M. Daum, R. Baral, H. E. Fischer, H. Cao, Y. Liu, M. B. Stone, J. A. Rodriguez-Rivera, E. S. Choi, Q. Huang, H. Zhou, M. Mourigal, and B. A. Frandsen, Phys. Rev. B **103**, 064424 (2021).

[32] Z. Hu, Z. Ma, Y.-D. Liao, H. Li, C. Ma, Y. Cui, Y. Shangguan, Z. Huang, Y. Qi, W. Li, Z. Y. Meng, J. Wen, and W. Yu, Nat. Commun. **11**, 5631 (2020).

[33] G. Hester, H. S. Nair, T. Reeder, D. R. Yahne, T. N. DeLazzer, L. Berges, D. Ziat, J. R. Neilson, A. A. Aczel, G. Sala, J. A. Quilliam, and K. A. Ross, Phys. Rev. Lett. **123**, 027201 (2019).

[34] S.-H. Jang, R. Sano, Y. Kato, and Y. Motome, Phys. Rev. Mater. **4**, 104420 (2020).

[35] F.-Y. Li, Y.-D. Li, Y. Yu, A. Paramekanti, and G. Chen, Phys. Rev. B **95**, 085132 (2017).

[36] Z.-X. Luo and G. Chen, SciPost Phys. Core **3**, 004 (2020).

[37] J. Xing, E. Feng, Y. Liu, E. Emmanouilidou, C. Hu, J. Liu, D. Graf, A. P. Ramirez, G. Chen, H. Cao, and N. Ni, Phys. Rev. B **102**, 014427 (2020).

[38] G. Sala, M. B. Stone, B. K. Rai, A. F. May, D. S. Parker, G. B. Halász, Y. Q. Cheng, G. Ehlers, V. O. Garlea, Q. Zhang, M. D. Lumsden, and A. D. Christianson, Phys. Rev. B **100**, 180406(R) (2019).

[39] Y. Hao, H. Wo, Y. Gu, X. Zhang, Y. Gu, S. Zheng, Y. Zhao, G. Xu, J. W. Lynn, K. Nakajima, N. Murai, W. Wang, and J. Zhao, Sci. China Phys. Mech. Astron. **64**, 237411 (2021).

[40] G. Sala, M. B. Stone, B. K. Rai, A. F. May, P. Laurell, V. O. Garlea, N. P. Butch, M. D. Lumsden, G. Ehlers, G. Pokharel, A. Podlesnyak, D. Mandrus, D. S. Parker, S. Okamoto, G. B. Halász, and A. D. Christianson, Nat. Commun. **12**, 171 (2021).

[41] Y. Matsumoto, S. Schnierer, J. A. N. Bruin, J. Nuss, P. Reiss, G. Jackeli, K. Kitagawa, and H. Takagi, Quantum critical Bose gas in the two-dimensional limit in the honeycomb antiferromagnet $YbCl_3$ under magnetic fields, arXiv:2207.02329 (2022).

[42] J. B. Fouet, P. Sindzingre, and C. Lhuillier, Eur. Phys. J. B **20**, 241 (2001).

[43] J. Merino and A. Ralko, Phys. Rev. B **97**, 205112 (2018).

[44] F. Ferrari and F. Becca, J. Phys.: Condens. Matter **32**, 274003 (2020).

[45] F. Ferrari, S. Bieri, and F. Becca, Phys. Rev. B **96**, 104401 (2017).

[46] C. Wessler, B. Roessli, K. W. Krämer, B. Delley, O. Waldmann, L. Keller, D. Cheptiakov, H. B. Braun, and M. Kenzelmann, npj Quantum Mater. **5**, 85 (2020).

[47] N. Niggemann, M. Hering, and J. Reuther, J. Phys.: Condens. Matter **32**, 024001 (2020).

[48] S. Gao, M. A. McGuire, Y. Liu, D. L. Abernathy, C. D. Cruz, M. Frontzek, M. B. Stone, and A. D. Christianson, Phys. Rev. Lett. **128**, 227201 (2022).

[49] T. Shimokawa, T. Okubo, and H. Kawamura, Phys. Rev. B **100**, 224404 (2019).

[50] H. Zhang and C. A. Lamas, Phys. Rev. B **87**, 024415 (2013).

[51] N. Caci, L. Weber, and S. Wessel, Phys. Rev. B **104**, 155139 (2021).

[52] D. Waibel, G. Fischer, T. Wolf, H. v. Löhneysen, and B. Pilawa, Phys. Rev. B **91**, 214412 (2015).

[53] Z. Zhang, Y. Cai, J. Kang, Z. Ouyang, Z. Zhang, A. Zhang, J. Ji, F. Jin, and Q. Zhang, Phys. Rev. Res. **4**, 033006 (2022).

[54] C. Tian, F. Pan, L. Wang, D. Ye, J. Sheng, J. Wang, J. Liu, J. Huang, H. Zhang, D. Xu, J. Qin, L. Hao, Y. Xia, H. Li, X. Tong, L. Wu, J.-H. Chen, S. Jia, P. Cheng, J. Yang *et al.*, Phys. Rev. B **104**, 214410 (2021).

[55] Z. Zhu, P. A. Maksimov, S. R. White, and A. L. Chernyshev, Phys. Rev. Lett. **120**, 207203 (2018).

[56] T. Paiva, R. T. Scalettar, W. Zheng, R. R. P. Singh, and J. Oitmaa, Phys. Rev. B **72**, 085123 (2005).

[57] W. Li, S.-S. Gong, Y. Zhao, and G. Su, Phys. Rev. B **81**, 184427 (2010).

[58] Y.-Z. Huang, B. Xi, X. Chen, W. Li, Z.-C. Wang, and G. Su, Phys. Rev. E **93**, 062110 (2016).

[59] R. Moessner and S. L. Sondhi, Phys. Rev. B **63**, 224401 (2001).

[60] T. Coletta, J.-D. Picon, S. E. Korshunov, and F. Mila, Phys. Rev. B **83**, 054402 (2011).

[61] L. Clark, G. Sala, D. D. Maharaj, M. B. Stone, K. S. Knight, M. T. F. Telling, X. Wang, X. Xu, J. Kim, Y. Li, S.-W. Cheong, and B. D. Gaulin, Nat. Phys. **15**, 262 (2019).

[62] Y. Li, Adv. Quantum Technol. **2**, 1900089 (2019).

[63] H. Bu, M. Ashtar, T. Shiroka, H. C. Walker, Z. Fu, J. Zhao, J. S. Gardner, G. Chen, Z. Tian, and H. Guo, Phys. Rev. B **106**, 134428 (2022).

[64] M. M. Bordelon, X. Wang, D. M. Pajerowski, A. Banerjee, M. Sherwin, C. M. Brown, M. S. Eldeeb, T. Petersen, L. Hozoi, U. K. Rößler, M. Mourigal, and S. D. Wilson, Phys. Rev. B **104**, 094421 (2021).

[65] M. Wu, D.-X. Yao, and H.-Q. Wu, Phys. Rev. B **103**, 205122 (2021).

[66] Y. Li, Q.-Y. Li, W. Li, T. Liu, D. J. Voneshen, P. K. Biswas, and D. Adroja, npj Quantum Mater. **6**, 34 (2021).

[67] J. Brgoch, C. K. H. Borg, K. A. Denault, A. Mikhailovsky, S. P. DenBaars, and R. Seshadri, Inorg. Chem. **52**, 8010 (2013).

[68] J. Rodríguez-Carvajal, Phys. B: Condens. Matter **192**, 55 (1993).

[69] T.-H. Jang, S.-H. Do, M. Lee, H. Wu, C. M. Brown, A. D. Christianson, S.-W. Cheong, and J.-H. Park, Phys. Rev. B **104**, 214434 (2021).

[70] F. Grußler, M. Hemmida, S. Bachus, Y. Skourski, H.-A. Krug von Nidda, P. Gegenwart, and A. A. Tsirlin, Phys. Rev. B **107**, 224416 (2023).

[71] Y. Tokiwa, S. Bachus, K. Kavita, A. Jesche, A. A. Tsirlin, and P. Gegenwart, Commun. Mater. **2**, 42 (2021).

[72] W. Xie, F. Du, X. Y. Zheng, H. Su, Z. Y. Nie, B. Q. Liu, Y. H. Xia, T. Shang, C. Cao, M. Smidman, T. Takabatake, and H. Q. Yuan, Phys. Rev. B **106**, 075132 (2022).

[73] G. R. Banjare, D. Bisen, N. Brahme, C. Belodhiya, and A. Upadhyay, IOP Conf. Ser.: Mater. Sci. Eng. **798**, 012010 (2020).

[74] G. A. Bain and J. F. Berry, J. Chem. Educ. **85**, 532 (2008).

[75] C. A. Pocs, P. E. Siegfried, J. Xing, A. S. Sefat, M. Hermele, B. Normand, and M. Lee, Phys. Rev. Res. **3**, 043202 (2021).

[76] A. Zorko, in *Topics From EPR Research*, edited by A. M. Maghraby (IntechOpen, Rijeka, 2018), Chap. 3.

[77] A. Abragam and B. Bleaney, *Electron Paramagnetic Resonance of Transition Ions* (Oxford University Press, New York, 2012).

[78] Y. Li, D. Adroja, R. I. Bewley, D. Voneshen, A. A. Tsirlin, P. Gegenwart, and Q. Zhang, Phys. Rev. Lett. **118**, 107202 (2017).

[79] L. Ding, P. Manuel, S. Bachus, F. Grußler, P. Gegenwart, J. Singleton, R. D. Johnson, H. C. Walker, D. T. Adroja, A. D. Hillier, and A. A. Tsirlin, Phys. Rev. B **100**, 144432 (2019).

[80] R. M. Moon, W. C. Koehler, H. R. Child, and L. J. Raubenheimer, Phys. Rev. **176**, 722 (1968).

[81] R. M. Moon, H. R. Child, W. C. Koehler, and L. J. Raubenheimer, J. Appl. Phys. **38**, 1383 (1967).

[82] L. Ortega-San Martin, J. P. Chapman, L. Lezama, J. Sánchez Marcos, J. Rodríguez-Fernández, M. I. Arriortua, and T. Rojo, Eur. J. Inorg. Chem. **2006**, 1362 (2006).

[83] J. Khatua, M. Pregelj, A. Elghandour, Z. Jagličic, R. Klingeler, A. Zorko, and P. Khuntia, Phys. Rev. B **106**, 104408 (2022).

[84] J. Kim, X. Wang, F.-T. Huang, Y. Wang, X. Fang, X. Luo, Y. Li, M. Wu, S. Mori, D. Kwok, E. D. Mun, V. S. Zapf, and S.-W. Cheong, Phys. Rev. X **9**, 031005 (2019).

[85] The relative intensity of the impurity signal with respect to the intrinsic signal becomes less since the T_1 of the nonmagnetic impurity signal becomes much longer than that of the intrinsic signal, making the impurity signal intensity much less.

[86] J. Khatua, S. Bhattacharya, Q. P. Ding, S. Vrtnik, A. M. Strydom, N. P. Butch, H. Luetkens, E. Kermarrec, M. S. Ramachandra Rao, A. Zorko, Y. Furukawa, and P. Khuntia, Phys. Rev. B **106**, 104404 (2022).

[87] M. Ulaga, J. Kokalj, A. Wietek, A. Zorko, and P. Prelovšek, Quantum spin liquid in the easy-axis Heisenberg model on frustrated lattices, arXiv:2307.03545.

[88] V. P. Bader, J. Langmann, P. Gegenwart, and A. A. Tsirlin, Phys. Rev. B **106**, 054415 (2022).

[89] C. Y. Jiang, Y. X. Yang, Y. X. Gao, Z. T. Wan, Z. H. Zhu, T. Shiroka, C. S. Chen, Q. Wu, X. Li, J. C. Jiao, K. W. Chen, Y. Bao, Z. M. Tian, and L. Shu, Phys. Rev. B **106**, 014409 (2022).

[90] R. Bag, M. Ennis, C. Liu, S. E. Dissanayake, Z. Shi, J. Liu, L. Balents, and S. Haravifard, Phys. Rev. B **104**, L220403 (2021).

[91] Y. Yamada and A. Sakata, J. Phys. Soc. Jpn. **55**, 1751 (1986).

[92] J. Wang, W. Yuan, T. Imai, P. M. Singer, F. Bahrami, and F. Tafti, Phys. Rev. B **103**, 214405 (2021).

[93] A. Chakraborty, V. Kumar, S. Bachhar, N. Büttgen, K. Yokoyama, P. K. Biswas, V. Siruguri, S. Pujari, I. Dasgupta, and A. V. Mahajan, Phys. Rev. B **104**, 115106 (2021).

[94] A. M. Clogston and V. Jaccarino, Phys. Rev. **121**, 1357 (1961).

[95] N. Li, Q. Huang, X. Y. Yue, W. J. Chu, Q. Chen, E. S. Choi, X. Zhao, H. D. Zhou, and X. F. Sun, Nat. Commun. **11**, 4216 (2020).

[96] G. Jackeli and G. Khaliullin, Phys. Rev. Lett. **102**, 017205 (2009).

[97] E. Lefrançois, M. Songvilay, J. Robert, G. Nataf, E. Jordan, L. Chaix, C. V. Colin, P. Lejay, A. Hadj-Azzem, R. Ballou, and V. Simonet, Phys. Rev. B **94**, 214416 (2016).

[98] S.-S. Gong, D. N. Sheng, O. I. Motrunich, and M. P. A. Fisher, Phys. Rev. B **88**, 165138 (2013).

[99] R. Ganesh, J. van den Brink, and S. Nishimoto, Phys. Rev. Lett. **110**, 127203 (2013).